Liquid flow and control without solid walls

Peter Dunne[1,2†], Takuji Adachi[1†], Alessandro Sorrenti[1,3], J.M.D. Coey[4], Bernard Doudin[2], Thomas M. Hermans[1,*]

Affiliations:

[1] University of Strasbourg, CNRS, ISIS UMR 7006, F-67000 Strasbourg, France
[2] University of Strasbourg, CNRS, IPCMS UMR 7504, 23 rue du Loess, F-67034 Strasbourg, France
[3] Institute for Chemical and Bioengineering, Department of Chemistry and Applied Biosciences, ETH Zürich, Vladimir Prelog Weg 1, 8093 Zürich, Switzerland
[4] School of Physics and CRANN, Trinity College Dublin, Dublin 2, Ireland
[*] Correspondence to: hermans@unistra.fr
[†] Equal contribution

Solid walls become increasingly important when miniaturizing fluidic circuitry to the micron scale or smaller.[1] They limit achievable flow-rates due to friction and high pressure drop, and are plagued by fouling[2]. Approaches to reduce the wall interactions have been explored using hydrophobic coatings[3,4], liquid-infused porous surfaces[4–6], nanoparticle surfactant jamming[7], changing the surface electronic structure[8], electrowetting[9,10], surface tension pinning[11,12], and atomically flat channels[13]. An interesting idea is to avoid the solid walls altogether. Droplet microfluidics achieves this, but requires continuous flow of both the liquid transported inside the droplets and the outer carrier liquid[14]. We demonstrate a new approach, where wall-less aqueous liquid channels are stabilised by a quadrupolar magnetic field that acts on a surrounding immiscible magnetic liquid. This creates self-healing, uncloggable, and near-frictionless liquid-in-liquid microfluidic channels that can be deformed and even closed in real time without ever touching a solid wall. Basic fluidic operations including valving, mixing, and 'magnetostaltic' pumping can be achieved by moving permanent magnets having no physical contact with the channel. This wall-less approach is compatible with conventional microfluidics, while opening unique prospects for implementing nanofluidics without excessively high pressures.

Magnetic forces have been used to avoid contact with the walls of a device by levitation of particles or live cells in suspension[15], and a first attempt to make wall-less microfluidic channels resulted in continuous 'magnetic antitubes' of water surrounded by an aqueous paramagnetic salt solution[16] using

a bulky electromagnet. However, the antitube lifetime was limited by ion interdiffusion between the two liquids, the salts were toxic, and contact with one stationary wall could not be avoided. Here we overcome all these limitations, creating entirely wall-less microfluidic channels consisting of diamagnetic antitubes completely enclosed by an immiscible, non-toxic paramagnetic fluid. The key magnetic confinement source design is made of a quadrupolar arrangement leading to nearly isotropic 2D confinement with a null magnetic field at the centre (Fig. 1a, 1b). Commercially available 6 x 6 x 50 mm $Nd_2Fe_{14}B$ magnets were used for linear channels, or else custom-made bilayers were waterjet cut to define more complex fluidic circuitry. The magnets were housed in a 3D printed support with conventional microfluidic inlet and outlet ports (Fig. 1a). The strength of the confinement depends on the magnetic susceptibility of the paramagnetic host fluid, so commercial ferrofluids were the natural choice, although their opacity severely limits optical characterisation. Aqueous antitubes were formed by pumping water into ferrofluid containing quadrupoles, and visualised by top-view X-ray imaging (Fig. 1c) or in side-view along the channel (Fig. 1d)[†]. To overcome the ferrofluid opacity, we developed a new class of rare-earth oil (see Methods), which we call 'Magoil' (Fig. 1e), inspired by diethylenetriaminepentaacetate-based contrast agents used for magnetic resonance imaging[17]. Antitubes could then be imaged using standard optical or fluorescent microscopy by adding some tracer (contrast ink or fluorescent dye, respectively) to the water antitube (Fig. 1f). Antitube extrusion and retraction can be visualised in real-time (movie S1), and they remain stable for months. Moreover, trapped gas bubbles that are often problematic in conventional devices can easily be removed, since their buoyancy in Magoil overcomes the magnetic confinement, and they rise to the oil/air interface whereas the liquid inside the antitube remains confined (cf. movie S1).

Our liquid-in-liquid design offers advantages of stability and robustness for fluid transport. Fig. 2A illustrates self-healing after an antitube in the ferrofluid was severed with a spatula. Recovery without applied external pressure is rapid, and it can even be observed in the magnetically weaker Magoil

[†] It is possible to stabilize air antitubes using ferrofluids as well.

(movie S2). The antitubes cannot be clogged: when glass beads are intentionally jammed into the antitube (Fig. 2b), they can be flushed out by a minimal applied pressure. Even a bead much larger than the antitube diameter can be pushed out using less than 10 mbar (Figs. 2c, 2d). The liquid walls of the antitube stretch to avoid clogging, and return to their original size when the obstruction is expelled. A change of external pressure alters the antitube size. In Extended Data Fig. 1 we show two extreme cases: antitubes remain unchanged with externally applied pressure for an open outlet (at atmospheric pressure), but dilate when the same pressure is applied with the outlet closed off. This can also be seen in Fig. 2c where the tube dilates behind the bead to accommodate the increased local pressure. In addition, ferrofluid surfaces have been shown to be anti-scaling[18] and resistant to biofilms[5].

At equilibrium, stable confinement of an antitube results from the competing magnetic energy of the confining fluid and the surface energy σ of the magnetic/nonmagnetic interface. These two energy densities, or effective pressures, inserted into the magnetically augmented version of Bernoulli's equation[19], give the equilibrium diameter of the antitube:

$$d = \frac{4\sigma}{2\mu_0 \overline{M} H_I + \mu_0 M_I^2} \tag{1}$$

where H_I, M_I are the magnetic field and magnetization values at the interface, and $\overline{M}$ is the field-averaged magnetization of the confining fluid induced by H_I. This simplified expression considers the magnetic pressure, $\frac{1}{2}\mu_0 H^2$, to be significantly larger than any difference in hydrostatic pressure (see supplementary text, section 1 for the derivation). Equation (1) can be linearized when $M = \chi H$, under the geometrical conditions $w \leq \frac{1}{2} h$, and $d \leq \frac{1}{2} w$, typical of our devices (see Fig. 1a). This linear model (LM) gives the minimum equilibrium dimensionless diameter $d^* = d/w$ as

$$d^* = \sqrt[3]{\frac{\pi^2}{N_D 2\chi(2\chi+1)}} \tag{2}$$

where $N_D = \frac{\mu_0 M_r^2 w}{\sigma}$ is the magnetic confinement number expressing the ratio of magnetic to surface energies (derivation in supplementary text, section 2). Note that a 1000-fold increase in χ reduces d^* by a factor 100, revealing how important the confining fluid properties are; the detailed dependence is plotted in Extended Data Fig. 2. At intermediate fields values, typical of our experimental conditions (Extended Data Fig. 3), significant deviation of the magnetization from linearity appears, and self-consistent solutions of Eq. (1) are obtained by numerical iteration, in our full model (FM) (see Extended Data Fig. 4 for computational algorithm).

Fig. 2e shows how the antitube diameter d changes with the dimensions of the magnetic flux source and the type of confining fluid. Good agreement is found between the experimental points for water antitubes and the predictions of Eqns. (1) and (2), using measured magnetization and interface energy (data in Extended Data: Table 1, Figs. 5, and 6). For ferrofluid tubes larger than 150 μm in ferrofluids, X-ray imaging can be used, while optical imaging of smaller tubes is possible in Magoil.

Miniaturization of the channels is possible thanks to an attractive feature of permanent magnets, namely that the fields they produce are *independent of length scale* ℓ. Hence H, M and the magnetic energy density do not depend on channel size. The interface energy σ however scales as ℓ^{-1}; with an oil/water interface energy of 23 mJ m^{-2}, a field of 100 mT and a susceptibility of 1, the antitube will become unstable below a diameter of 5 μm (Extended Data Fig. 7). Further miniaturization would require σ to be reduced, which is possible by using a surfactant as illustrated in Fig. 2e (red and orange curves), and Extended Data Fig. 2 (white circles). By combining a very strong ferrofluid (QK100 with a magnetisation of 100 kA m^{-1} in a hydrocarbon medium) and a double surfactant approach (e.g., Span-80[20] in the ferrofluid, and Tween-20 in the aqueous antitube), we estimate that antitube diameters of ~100 nm could ultimately be achieved. Though difficult to image, such nanometer-sized antitubes would allow practical nanofluidic devices to be realized.

A key advantage of liquid-in-liquid flow is the frictionless transport and negligible pressure drop. A dramatic illustration is shown in Fig. 3a and movie S3, where flow of a magnetically confined antitube

made of honey is compared to honey flow in a standard tube. Here, we observed an antitube flow of 39.4 ± 0.7 g/hour, 70 times faster than through a conventional plastic tubing of the same diameter d = 1.1 mm, (0.55 ± 0.11 g/hour). This is equivalent to Poiseuille flow of honey through a plastic tube with a diameter 3 times larger than the antitube. The ferrofluid acts as a lubricating layer, with an effective slip length at the honey/ferrofluid boundary that can be approximated by[21]

$$b = t_f \left(\frac{\mu_h}{\mu_f} - 1 \right) \tag{3}$$

where t_f is the thickness of ferrofluid between the honey and solid wall (~1.45 mm), μ_h and μ_f are the kinematic viscosities of honey and ferrofluid respectively, giving a slip length 480 mm. When b/d > 5 the velocity profile is essentially plug-like. Remarkably, the flow rate of honey through the antitube was 1.5 times faster than when there was no tube, likely due to competition between orifice wetting[22] and the higher hydrostatic pressure due to the greater height of the honey column in the antitube design.

Fig 3b shows a 1 m long quadrupole built using 80 magnets, mounted and glued in 20 3D-printed segments. A water antitube was easily formed and water flows freely through it. Since it is a transparent cylinder surrounded by ferrofluid, it acts as an optical waveguide (Fig. 3c). Exotic tube cross-sections can be achieved by further iteration of the initial quadrupole design, leading to novel flow geometries. For example, four bar magnets pointing in the same direction produce a double lobe antitube (Fig. 3b, and movie S4) and a circular arrangement of six magnets yields an asymmetric triple antitube (Fig. 3b, and movie S5), in agreement with calculations. As there are innumerable possible magnet arrangements[23], this result demonstrates a promising aspect of magnetic confinement.

All essential functions required to control microfluidic flow can be implemented with aqueous antitubes (Fig. 4). Valves can be constructed by adding a magnet whose axis of magnetization is perpendicular to the quadrupole axis. These valving magnets simply pinch off the antitube by removing the null field at the centre (Fig. 4a, 4b), thus interrupting the liquid flow (see movies S6 – S8). A single transverse valving magnet was able to sustain an excess pressure of 125 mbar, whereas a symmetric dual valve (Fig. 4c) withstood 300 mbar. Pumping arises as an extension of the valving principle; travelling pinch

points can be created by mechanical magnet displacement or by sequential excitation of electro- or electro-permanent magnets. A proof-of-principle using six transverse valving magnets attached to a rotor, enables the pinch point to travel along the channel at 10 – 100 mm s^{-1} (Fig. 4d, movie S9), resulting in magnetostaltic flow, similar to that produced by a peristaltic pump. A pumping pressure of 20 mbar and flow rates of 500 μL min^{-1} were achieved (Fig. 4e, 4f) in antitubes with d = 500 μm. This method has significant advantages compared to traditional external peristaltic pumps as it can be implemented on-chip and does not create mechanical wear on a tube.

We have also demonstrated the applicability of magnetic confinement to more complicated fluidic circuitry. A quadrupole fluidic device was prepared by first assembling two $Nd_2Fe_{14}B$ plates that are perpendicularly magnetized in opposite directions (Fig. 4g). Any desired shape of channel can be cut, and the null-field line follows the track centre. In-plane quadrupoles are different (cf. Fig. 1); there the direction of the channels within the plane should make an angle $\gtrsim 30°$ to the magnetic axis (Extended Data Figs. 8–10). Symmetric splitting of the flow was demonstrated in a ferrofluid antitube Y-junction (movie S10). Merging of the flow at a Y-junction was visualized using antitubes stabilized by Magoil (Fig. 4h). Remarkably, the mixing occurs immediately after the Y-junction due to a Kelvin-Helmholz instability[16]. This is in striking contrast to the laminar flow observed in a 3D printed microfluidic chip with the same channel size and geometry as the antitube (Fig. 4i).

The near-perfect slip conditions at the liquid wall lead to the unusual fluidic behaviour we have observed at the sub-mm scale, where the flow in conventional devices would necessarily be laminar. The magnetic control of basic microfluidic functions that we have implemented clears the path for fully-integrated antitube fluidics. We envisage that miniaturized fluidic circuits with no solid walls will be scalable down to submicron sizes, enabling better control over transport of matter at the nanoscale.

References:

1. Tabeling, P. *Introduction to Microfluidics*. (OUP Oxford, 2005).
2. Mukhopadhyay, R. When Microfluidic Devices Go Bad. *Anal. Chem.* **77,** 429 A-432 A (2005).

3. Zhao, B., Moore, J. S. & Beebe, D. J. Surface-Directed Liquid Flow Inside Microchannels. *Science* **291,** 1023–1026 (2001).

4. Wong, T.-S. *et al.* Bioinspired self-repairing slippery surfaces with pressure-stable omniphobicity. *Nature* **477,** 443–447 (2011).

5. Wang, W. *et al.* Multifunctional ferrofluid-infused surfaces with reconfigurable multiscale topography. *Nature* (2018). doi:10.1038/s41586-018-0250-8

6. Leslie, D. C. *et al.* A bioinspired omniphobic surface coating on medical devices prevents thrombosis and biofouling. *Nat. Biotechnol.* **32,** 1134–1140 (2014).

7. Forth, J. *et al.* Reconfigurable Printed Liquids. *Adv. Mater.* 1707603 (2018). doi:10.1002/adma.201707603

8. Secchi, E. *et al.* Massive radius-dependent flow slippage in carbon nanotubes. *Nature* **537,** 210–213 (2016).

9. Banerjee, A., Kreit, E., Liu, Y., Heikenfeld, J. & Papautsky, I. Reconfigurable virtual electrowetting channels. *Lab. Chip* **12,** 758 (2012).

10. Choi, K., Ng, A. H. C., Fobel, R. & Wheeler, A. R. Digital Microfluidics. *Annu. Rev. Anal. Chem.* **5,** 413–440 (2012).

11. Lee, W. C., Heo, Y. J. & Takeuchi, S. Wall-less liquid pathways formed with three-dimensional microring arrays. *Appl. Phys. Lett.* **101,** 114108 (2012).

12. Walsh, E. J. *et al.* Microfluidics with fluid walls. *Nat. Commun.* **8,** 816 (2017).

13. Keerthi, A. *et al.* Ballistic molecular transport through two-dimensional channels. *Nature* **558,** 420–424 (2018).

14. Shang, L., Cheng, Y. & Zhao, Y. Emerging Droplet Microfluidics. *Chem. Rev.* **117,** 7964–8040 (2017).

15. Zhao, W., Cheng, R., Miller, J. R. & Mao, L. Label-Free Microfluidic Manipulation of Particles and Cells in Magnetic Liquids. *Adv. Funct. Mater.* **26,** 3916–3932 (2016).

16. Coey, J. M. D., Aogaki, R., Byrne, F. & Stamenov, P. Magnetic stabilization and vorticity in submillimeter paramagnetic liquid tubes. *Proc Natl Acad Sci* **106,** 8811–8817 (2009).

17. Caravan, P., Ellison, J. J., McMurry, T. J. & Lauffer, R. B. Gadolinium(III) Chelates as MRI Contrast Agents: Structure, Dynamics, and Applications. *Chem. Rev.* **99,** 2293–2352 (1999).

18. Masoudi, A., Irajizad, P., Farokhnia, N., Kashyap, V. & Ghasemi, H. Antiscaling Magnetic Slippery Surfaces. *ACS Appl. Mater. Interfaces* **9,** 21025–21033 (2017).

19. Rosensweig, R. E. *Ferrohydrodynamics*. (Dover Publications, 2014).

20. Posocco, P. *et al.* Interfacial tension of oil/water emulsions with mixed non-ionic surfactants: comparison between experiments and molecular simulations. *RSC Adv* **6,** 4723–4729 (2016).

21. Choi, C.-H. & Kim, C.-J. Large Slip of Aqueous Liquid Flow over a Nanoengineered Superhydrophobic Surface. *Phys. Rev. Lett.* **96,** 066001 (2006).

22. Ferrand, J., Favreau, L., Joubaud, S. & Freyssingeas, E. Wetting Effect on Torricelli's Law. *Phys. Rev. Lett.* **117,** 248002 (2016).

23. Furlani, E. P. *Permanent Magnet and Electromechanical Devices*. (Academic Press, 2001).

Acknowledgments: We acknowledge the support of the University of Strasbourg Institute for Advanced Studies (USIAS) Fellowship, The Chaire Gutenberg of the Région Alsace (J.M.D.C.), the Labex NIE 11-LABX-0058_NIE within the Investissement d'Avenir program ANR-10-IDEX-0002-02, and SATT Conectus funding. We are grateful to Dr. Hu Boping, of San Huan Corporation for giving us thin magnetic bilayer sheets.

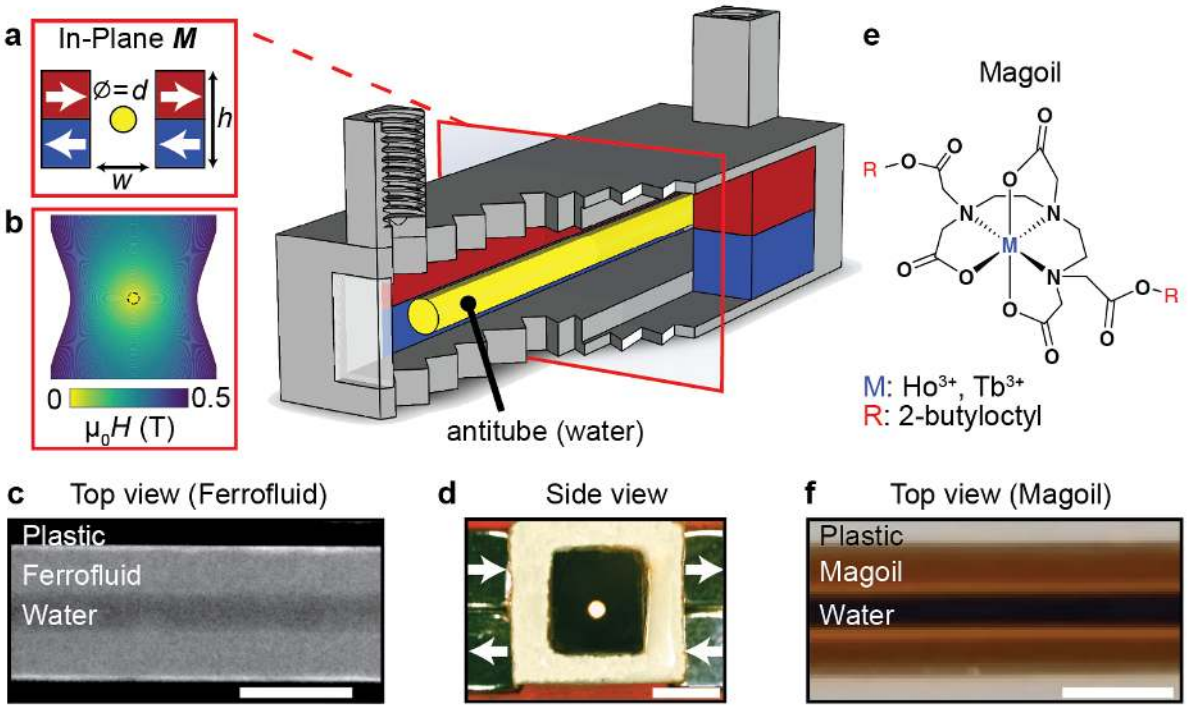

Fig. 1 | **Wall-less magnetic confinement of liquids.** Centre: exploded view of the fluidic cell, made of: **a** permanent magnets (red, blue) in an in-plane quadrupolar configuration creating a low-field zone, at the centre where a tube of water (yellow) is stabilized inside a magnetic immiscible liquid; **b** contour plot of the magnetic field; **c** X-ray transmission top-view of a water antitube in ferrofluid; **d** optical side-view of a water antitube in ferrofluid; **e** chemical formula of the transparent paramagnetic oil called 'Magoil' (with Ho^{3+} unless otherwise specified); and **f** optical top-view of a water antitube (dyed black for contrast) in Magoil. The scale bars are 5 mm.

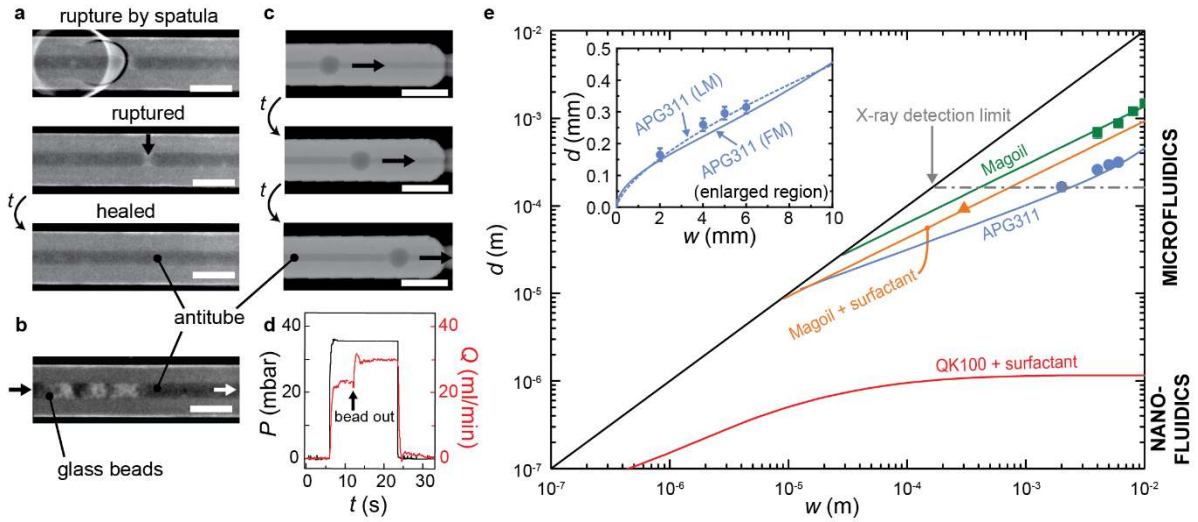

Fig. 2 | Robustness, self-healing, and scaling of water antitubes. a Top-view X-ray images illustrating the mechanical rupture of a tube using a spatula, self-healing by returning to equilibrium within minutes; **b** 600 μm glass beads jammed into a 1.5 mm antitube that can be expelled with a slight increase in applied pressure; **c** a 2 mm diameter bead larger than the antitube diameter (d = 0.5 mm) does not cause clogging. **d** a small increase in flow rate is observed after the bead (of panel C) leaves the antitube; **e** Water antitube diameter d versus gap width w. Points are experimental data (cf. Extended Data Figs. 12, 13 for method of width determination), lines are calculated from Equs (1,2): for Magoil (LM), Magoil with 1% Tween-20 surfactant (cf. Extended Data Fig. 13) in the water (LM), and APG311 (FM). The red curve shows the FM model outcome with a very strong ferrofluid (QK100, 100 kA m^{-1}) and where the surface tension σ is lowered to 1 mN m^{-1} using surfactants (e.g., Tween-20 and Span-80). The inset shows an enlarged area for APG311 data points and error bars from at least three independent experiments.

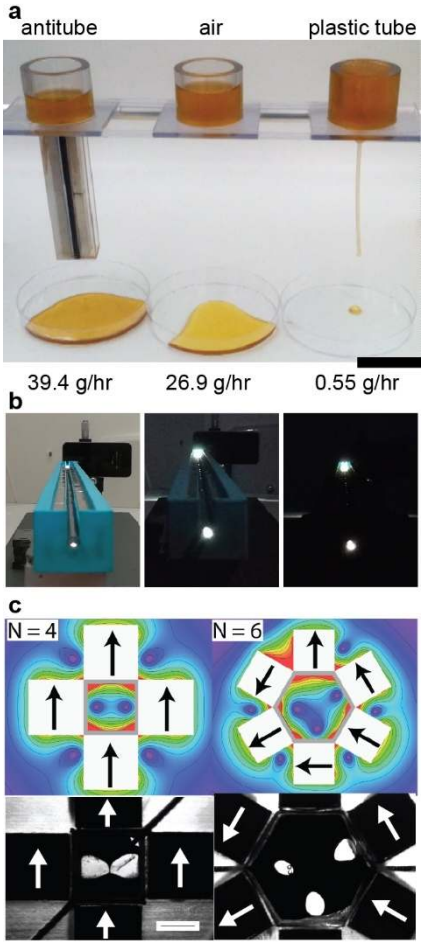

Fig. 3 | Special features of magnetic confinement. a Comparative flow of honey under gravity through an antitube, no tube (i.e., air only), and a normal tube of the same diameter (see movie S3): **b** Side-view of a 1 m long water antitube (d = 2 mm), used as a light waveguide, shown at three ambient light intensities; **c** unique antitube cross-sections using variations of the design of Fig. 1 for various magnet arrangements. Top show simulations, bottom experiments. Scale bar is 3 mm (see movies S4, S5).

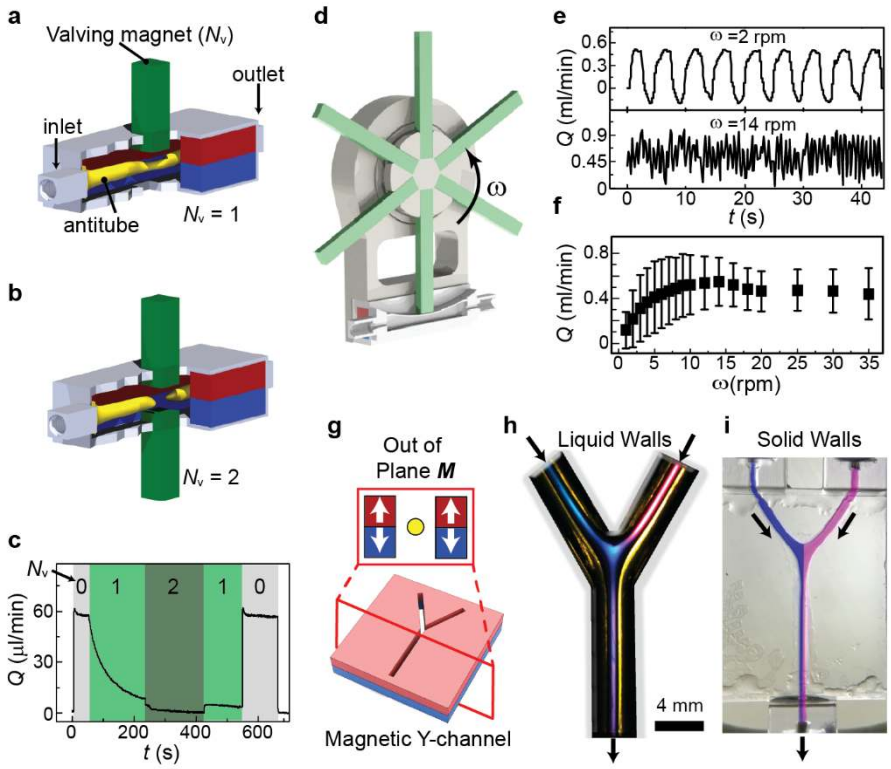

Fig. 4 | Magnetically implemented fluidic functionalities. Simulated valving of an antitube (in yellow) using additional valving magnets (green) **a** one magnet (N_v = 1, see movie S7), **b** two magnets (N_v = 2, see movie S8); **c** measured flow rate at the exit port upon addition and removal of 1 or 2 valving magnets, **d** cross-sectional schematic of a peristaltic pump using a six-armed wheel rotating at angular frequency ω in close proximity to a quadrupole (see movie S9); **e** Slow rotation (2 rpm) leads to pulsed flow, while fast rotation (14 rpm) produces a smoother flow; **f** the average flow rate and standard deviation vs. rotation rate ω; **g** out of plane magnetization configuration for a waterjet cut Y-junction in two magnets; **h** optical image of a Tb^{3+}–Magoil stabilised aqueous antitube, where blue and pink dye are flowed into the inlets (300 µL min^{-1}), and mix immediately upon contact before flowing towards the outlet (cf. magnetic contours in Extended Data Fig. 11). **i** 3D printed comparison track with solid walls at the same flow rate (as panel h) exhibiting laminar flow and no convective mixing.